ADVANCES IN PLANAR MATHEMATICAL ABSORBER REFLECTION SUPPRESSION

Stuart Gregson, Allen Newell, Greg Hindman
Nearfield Systems Inc.
19730 Magellan Drive,
Torrance, CA 90502-1104

ABSTRACT

When making antenna measurements, great care must be taken in order to obtain high quality data. This is especially true for near-field antenna measurements as a significant amount of mathematical post-processing is required in order that useful far-field data can be determined. However, it is often found that the integrity of these measurements can be compromised in a large part through range reflections, *i.e.* multipath [1]. For some time a technique named Mathematical Absorber Reflection Suppression (MARS) has been used to reduce range multi-path effects within spherical [2, 3], cylindrical [4, 5] and most recently planar [6, 7] near-field antenna measurement systems. This paper presents the results of a recent test campaign which yields further verification of the effectiveness of the technique together with a reformulation of the post-processing algorithm which, for the first time, utilises a rigorous spherical wave expansion based orthogonalisation and filtering technique.

Keywords: Reflection Suppression, Planar Near-field, Antenna Measurements, Spherical Wave Expansion.

1.0 Introduction

When making indoor antenna measurements, unwanted reflections are largely suppressed by lining the exposed surfaces of the interior of the test chamber and test equipment with electromagnetic anechoic material. Such material, which typically comprises open cell Carbon loaded foam, can be costly, bulky, delicate, and over time can tend to shed particles of Carbon. Most absorber is shaped specifically so that its performance is optimised for use across a predetermined range of frequencies which necessarily render it less effective at other frequencies. Whilst considerable effort can be devoted to optimising the design and placement of absorber within the test environment, it is not possible to place this material everywhere, and some surfaces are inevitably left exposed, *e.g.* linear bearings, lights, *etc.*. Although many different multipath suppression techniques have been proposed for use with planar near-field antenna measurement systems with notable examples including: hardware and software time-gating, aperture plane spatial filtering, background subtraction, circular complex plane least-squares fitting, and signal correlation based techniques; it is only very recently that the highly effective and very general mode orthogonalisation and filtering based techniques [2, 3, 4, 5] have been successfully extended to the planar geometry [6, 7]. The purpose of this investigation has been to further develop and refine the novel planar mathematical absorber reflection suppression (P-MARS) measurement and post-processing technique and to obtain further verifications of its effectiveness. This paper commences by presenting an overview of the P-MARS measurement technique and the novel post-processing algorithm. Previously, the requisite modal orthogonalisation and filtering has been accomplished by expanding the fields onto a set of cylindrical modes in a source-free region of space [6, 7]. Whilst this data processing technique has been shown to be a highly effective and efficient strategy for implementing the processing, this paper will show how the processing can be accomplished rigorously by recasting the problem in terms of a spherical wave expansion (SWE). Obtaining equivalent results from an entirely independent algorithm offers a powerful method for verifying and validating the implementation of the planar MARS post-processing algorithm with the use of spherical modes providing the additional benefit of enabling two-dimensional mode orthogonalisation and filtering to be applied as part of a single operation without recourse to approximation, which was previously a requirement. The new SWE based processing yields a clear advantage over the corresponding cylindrical mode implementation which required the processing to be applied twice, that is, once for each of the orthogonal axes. This paper then proceeds to address the spatial and angular sampling and filtering requirements of the new P-MARS technique. A clear understanding of these is essential if reliable, efficient, measurements and processing are to be achieved.

2.0 Introduction to P-MARS

From classical electromagnetic theory it is well know that any given field can be represented as a linear combination of any complete set of suitable basis functions where these functions (*i.e.* "modes") are taken to constitute exact analytic solutions of Maxwell's equations. By selecting free-space elemental solutions of Maxwell's equations is it possible to expand a monochromatic free-field onto a set of plane, cylindrical or spherical vector mode coefficients. As these modes are essentially a mathematical convenience, rather than a physical reality, it is possible to convert between bases

although a significant degree of mathematical convenience is obtained if the modes are matched to fields across a commensurate bounding surface. This concept has been used as the basis of many near-field to far-field transformation algorithms. In principle, it is possible to obtain spherical mode coefficients (SMC) or cylindrical mode coefficients (CMC) from the plane wave spectrum (PWS) by using the field equivalence principle and by matching fields outside the excluded region [6]. This is most readily accomplished by equating fields in the far-field region and, as reactive *i.e.* evanescent, fields are not sampled when taking near-field measurements, no loss of precision or generality is incurred in adopting this strategy. This conversion of bases offers one new strategy for implementing scattering suppression techniques with planar near-field antenna measurements. The remainder of this section is devoted to the development of this post-processing methodology.

Probe pattern corrected far electric fields can be obtained directly from planar near-field measurements tabulated on a polar spherical co-ordinate system by carefully selecting the appropriate direction cosines [8]. Thus, the angular spectrum can be obtained directly from the sampled tangential orthogonal near-field components using,

$$\underline{F}_T(k_x,k_y,z=0) = \int_{-\infty}^{\infty}\int_{-\infty}^{\infty} \underline{E}_T(x,y,z=0)e^{j(k_x x + k_y y)}dxdy \qquad (1)$$

Here, $\underline{E}_T$ denotes the two tangential orthogonal sampled near-field components, $k_x = k_0\sin\theta\cos\phi$, $k_y = k_0\sin\theta\sin\phi$, $k_z = k_0\cos\theta$ where θ and ϕ are used to denote the conventional polar and azimuthal spherical angles, and k_0 is the free space propagation constant. Generally the measured spectral components are corrected for the directive and polarisation properties of the near-field probe. In order that polar spherical far electric fields can be calculated, the spherical angles are determined using a lattice of points that is plaid, monotonic and equally spaced in θ and ϕ. Probe pattern correction is not the subject of this paper and a detailed discussion can be found in the open literature, *e.g.* [8, 9] however its omission from this analysis is not a limitation of the technique and probe corrected results are presented throughout. The propagating far electric field can be obtained from the tangential angular spectra using the method of stationary phase and the plane wave condition [8]. Thus, as $r \to \infty$,

$$\underline{E}(k_x,k_y) \approx j\frac{e^{-jk_0 r}}{\lambda r}\frac{k_z}{k_0}\left[\underline{F}_T(k_x,k_y) - \frac{k_T \cdot F_T(k_x,k_y)}{k_z}\hat{\underline{e}}_z \right] \qquad (2)$$

As all three Cartesian components of the far electric field are know, it is a trivial matter to resolve these fields onto a polar spherical polarisation basis using [8],

$$\begin{bmatrix} E_\theta \\ E_\phi \end{bmatrix} = \begin{bmatrix} \cos\theta\cos\phi & \cos\theta\sin\phi & -\sin\theta \\ -\sin\theta & \cos\phi & 0 \end{bmatrix} \cdot \begin{bmatrix} E_x \\ E_y \\ E_z \end{bmatrix} \qquad (3)$$

Where,

$$\underline{E}(\theta,\phi) = E_\theta(\theta,\phi)\hat{\underline{e}}_\theta + E_\phi(\theta,\phi)\hat{\underline{e}}_\phi \qquad (4)$$

For all of the MARS implementations, once the probe corrected far electric fields have been determined using standard near-field theory, the AUT is mathematically translated back to the origin of the measurement frame of reference through the application of a differential phase change [4, 6, 7, 10], *i.e.*,

$$\underline{E}_t(r\to\infty,\theta,\phi) = \underline{E}(r\to\infty,\theta,\phi)e^{jk_0 \cdot \underline{r}} \qquad (5)$$

Here, $\underline{r}$ denotes the displacement vector between the centre of the measurement co-ordinate system and the centre of the current sources *e.g.* the aperture of the AUT. This has the corresponding effect of reducing the number of mode coefficients, of any elementary kind, that are required to represent that field. That is, we have reduced the maximum radial extent (MRE) [10] to a conceptual (*i.e.* optimised) minimum value allowing all higher order modes to be filtered out using an appropriate filter function without compromising the integrity of the underlying antenna pattern function. This concept is discussed in greater detail in the following section.

The electromagnetic fields outside an arbitrary test antenna radiating into free space can be expanded onto a set of elementary orthogonal spherical mode coefficients (SMCs) whereupon these vector mode functions and associated mode coefficients can then be used to obtain the electric and magnetic fields everywhere in space outside of a conceptual spherical surface of radius ρ_0 which encloses that radiator. Specifically, in a source or sink free simple linear homogeneous and isotropic region of space which is bounded by spherical surfaces and is centred at the origin of a spherical co-ordinate system, the electric field can be expressed as [10],

$$\underline{E}(r,\theta,\phi) = k_0\sqrt{Z}\sum_{n=1}^{\infty}\sum_{m=-n}^{n}\left[Q_{TEmn}^{(3)}\underline{F}_{TEmn}^{(3)}(r,\theta,\phi) \right. \qquad (6)$$
$$\left. + Q_{TMmn}^{(3)}\underline{F}_{TMmn}^{(3)}(r,\theta,\phi) \right]$$

Here, $Q_{TEmn}^{(3)}$ and $Q_{TMmn}^{(3)}$ are used to denote the transverse electric (with respect to the radial co-ordinate) and transverse magnetic wave coefficients, which are complex functions of m and n, $\underline{F}_{TEmn}^{(3)}$ and $\underline{F}_{TMmn}^{(3)}$ are, respectively, the transverse electric and transverse magnetic spherical vector wave-functions which are dimensionless functions of m, n, r, θ, ϕ and in all cases the superscript (3) indicates spherical Hankel functions which represent radial outgoing waves that satisfy the radiation condition. The intrinsic impedance of the medium through which the field is propagating is denoted by Z. In practice the n-summation of the spherical wave expansion has to be truncated at some finite value, say N, which is sufficiently large to insure that the properties of the field have been accurately and precisely represented. As it was assumed in the formulation that the majority of

the current sources are located within a sphere of radius ρ_0, spherical waves of order $N > k_0\rho_0$ represent the most complex constituents of the field structure thus typically N is chosen so that,

$$N = \mathrm{ceil}(k_0\rho_0) + n_1 \qquad (7)$$

Here, ceil is used to denote a function that rounds to the nearest integer towards positive infinity, n_1 is a positive integer that depends upon the accuracy required (*e.g.* $n_1 = 10$). When deriving cylindrical mode coefficients from planar near-field antenna measurements, it was found that the MRE was related to the maximum dimension of the acquisition plane [6, 7]. That is, the highest order mode coefficient was related directly to the size of the near-field sampling interval. Using equation (7), this implies that for the complete spherical mode set to be calculated that represents the planar *measured* data, the maximum number of polar modes is,

$$N = \mathrm{ceil}\!\left(k_0\sqrt{x_{span}^2 + y_{span}^2}\Big/2\right) + n_1 \qquad (8)$$

Here, x_{span} and y_{span} are the *x*- and *y*-axis planar near-field measurement spans respectively. Conventional spherical near-field theory states that the polar sample spacing is related to the maximum mode index using [10],

$$\Delta\theta = \frac{2\pi}{2N+1} \qquad (9)$$

Thus when determining SMCs from planar near-field antenna measurements the polar sample spacing is required to be no less than,

$$\Delta\theta = \frac{2\pi}{2\left(\mathrm{ceil}\!\left(k_0\sqrt{x_{span}^2 + y_{span}^2}\Big/2\right) + n_1\right) + 1} \qquad (10)$$

Providing the planar near-field measurement is correctly spatially sampled, it is possible to compute far-field data that is tabulated across an arbitrarily finely sampled grid with no additional experimental burden. The ϕ-axis sample spacing can be obtained in a similar fashion however here the maximum radial extent referrers to the radius of a circular cylinder that is centred about the *z*-axis of the range (*i.e.* at a normal to the scan plane) and that is large enough to encompass the majority of the current sources. In the example discussed below, the two MREs are the same and as such and the θ and ϕ axis increments are equal. Thus, by using equations, (1 - 6) it is therefore possible to obtain SMCs from a planar-near field measurement in a rigorous way, that is to say without recourse to approximation. The process is: 1- Measure planar near-field data on a plane offset from the origin, 2- Calculate the theta and phi components of the far-field on a θ, ϕ grid, 3- Calculate the SMCs for this far-field data.

SMCs are complex numbers that are functions of the polarization index, and the *n, m* index. Figure 1 and

Figure 2 present false colour (checkerboard) plots of the amplitudes of the TE and TM SMCs which were obtained from a planar near-field measurement by using the data processing chain described above.
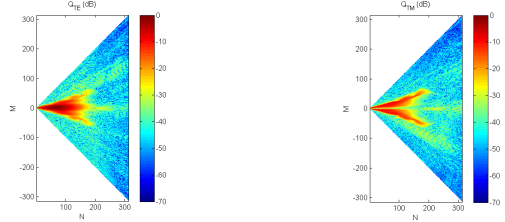

Figure 1 – TE SMCs derived from planar near-field measured data where z > 0.

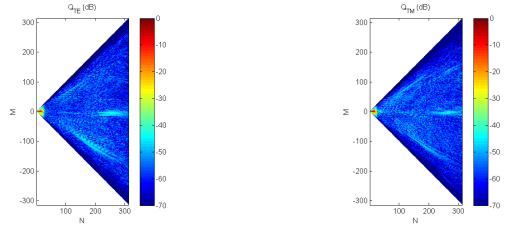**Figure 2 – TM SMCs derived from planar near-field measured data where z > 0.**

Figure 3 – TE SMCs for AUT translated to the origin derived from PNF data.

Figure 4 – TM SMCs for AUT translated to the origin derived from PNF data.
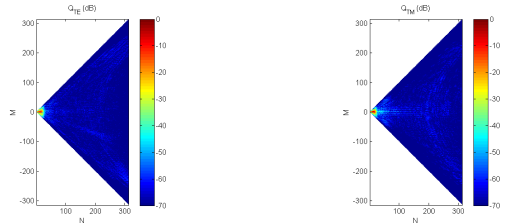

Figure 5 – TE SMCs for AUT located at origin derived from PNF data, no scatterer.

Figure 6 – TE SMCs for AUT located at origin derived from PNF data, no scatterer.

In each of these plots, modes for which $|m| > n$ are (mathematically) undefined are represented with white space. The offset in the near-field measurement between the AUT and the probe causes the phase of the measured signals to vary more rapidly across the measurement plane and produce the broad distribution of modes shown in Figures 1 and 2, *i.e.* modes with significant amounts of power for higher order *m* and *n* indices. Conversely, Figures, 3 and 4 contain equivalent plots only in this case, the AUT has been mathematically translated back to the origin of the measurement co-ordinate system prior to the computation of the SMCs. Here, it is quite evident that as a direct consequence of this translation the AUT pattern is now represented by far fewer, lower order, SMCs than would otherwise have been the case. The modes associated with the AUT are within a very small region at the "tip" of the plots in Figures 3 and 4 (*i.e.* where *m* and *n* are small). However, and as has been the case for all other implementations of MARS, those modes associated with room scattering effects (which are spatially extended) can be seen to be represented by higher order mode coefficients. These appear as low level "trails" in

the regions beyond the tip in Figures 5 and 6. This is evident from inspection of Figure 5 and 6 where the "trails" outside the "tip" are abscent. These SMCs were obtained from the same experimental setup that was used to generate the data presented in Figures 3 and 4 only in this instance a large scattering object was removed from the chamber prior to taking the near-field data. In effect, the contributions in the SMC domain of the AUT and the scatterers are separated so that they do not interfere and are effectively orthogonalised from one another. Thus, by filtering out the higher order modes that cannot be associated with the AUT itself, which can be calculated based upon knowledge of the physical size of the antenna and the associated mode cut-off number, room scattering can be suppressed. Hence, any coefficients outside of the $k_0 r_{t0}$ region of mode space can be removed without prejudice to the underlying far-field antenna pattern function. Here, r_{t0} denotes the conceptual minimum possible MRE that just circumscribes the AUT. Once the filtered SNCs are obtained, the far-field pattern can be obtained using standard efficient spherical processing. Although the filtering is normally based on the size of the antenna this may be increased for analysis purposes up to a limit determined by the angular sample spacing. Crucially, for the planar MARS implementation, this angular spacing can be freely specified by the user and is completely independent of the x-, y- near-field sample spacing. It is clear that the SMCs associated with the AUT are confined to a region that is tightly distributed about low order polar modes. As the total power radiated by the AUT must be conserved, the amount of power per mode must increase as the total number of modes associated with the AUT decreases. As the amount of noise per mode can be seen to be roughly constant, in this case at circa -50 dB with respect to the maximum level, the effective system signal to noise ratio (SNR) of the measurement is significantly increased through this processing. Planar testing is known to admit greater and greater amounts of spurious noise into the measurement as the scan plane is progressively enlarged (as is required when testing wide-out sidelobes) however P-MARS processing can be seen to provide a highly effective method of compensating for this undesirable, and frequently encountered, effect.

3. Verification of P-MARS Post Processing

Experimental verification of the P-MARS measurement technique has primarily been based upon assessing the repeatability between successive measurements where a single parametric change had been introduced in the experimental configuration and by assessing the degree of agreement between the processed results. The intent being to demonstrate that the P-MARS processing is capable of compensating for a given change in the experimental setup. Figure 7 below shows a NSI-300V-12x12, 12'×12' vertical planar near-field system installed within a partially absorber lined chamber. The first measurements consisted of taking a baseline acquisition after which a large aluminium scatterer was placed in the region of greatest field intensity on the rear wall immediately behind the centre of the scan plane. This arrangement can be seen presented in Figure 7. This was intended to introduce a large, worst-case, specular reflection into the measured antenna radiation pattern so that the effects of the P-MARS processing could be clearly observed and easily verified.

Figure 7 – NSI-300V-12x12 system shown with reflector placed behind near-field measurement scan plane measuring *x*-band SGH

Figure 8 presents the far-field pattern obtained from conventional planar processing of the scattering contaminated measurements taken of an *x*-band standard gain horn (SGH), as pictured above. Here, a great deal of spurious high angular frequency ripple is evident on the pattern together with an additional large amplitude refection, all of which are artefacts of the scatterer that has been placed behind the scan plane.
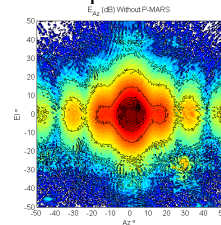

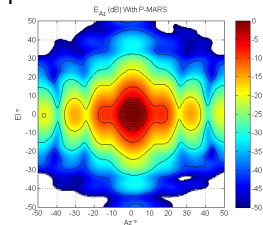**Figure 8 – Measurement with reflector on back wall. Far-field pattern without P-MARS**

Figure 9 – Measurement with reflector on back wall. Processed using P-MARS gen 1

Figure 9 presents an equivalent plot of the same measured data after conventional cylindrical mode based P-MARS (first generation) processing has been applied [6, 7]. Clearly, the spurious high angular frequency ripple has been effectively eradicated together with the spurious large amplitude scattering that is clearly evident on the unfiltered results in the region $Az = 25°$, $El = -25°$. Figure 11 contains an equivalent antenna diagram only here, the planar MARS processing has been implemented using the spherical mode based processing described above, termed second generation P-MARS processing. The resulting MARS processed far-fields that have been obtained using the first and second generations of the planar MARS are clearly in very encouraging agreement with one another with the scattering being very effectively suppressed in both. In order that the degree of

agreement could be further verified, contour (iso-level) pattern plots were overlaid where the contours were plotted at the -40, -30, -20, -10, -5, -4, -3, -2 dB levels with each pattern being normalised to 0 dB at the peak of the pattern. Here, red contours are used to represent first generation P-MARS processed results, whilst black contours are used to denote second generation P-MARS results. Again, the degree of agreement is encouraging with contours being in good agreement down to the -40 dB level over all angles. Some small differences are evident and these are largely a result of the difference between the included region respectively by the cylindrical (first generation) and spherical (second generation) implementations. The cylindrical based processing uses the intersection of two orthogonal right circular cylindrical surfaces to define the included region, whereas the spherical based processing uses a single spherical surface to define the included region. As these two regions of space are subtly different, and as the degree of scattering is severe, some small differences are expected.
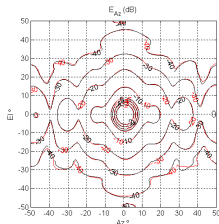

Figure 10 – Comparison of P-MARS version 1 and P-MARS version 2.
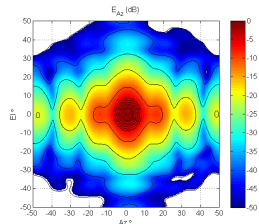

Figure 11 – Measurement with reflector on back wall. Processed using P-MARS gen 2

That being noted, the degree of agreement obtained is very encouraging which is significant as the respective mathematical formulations and computational implementations are entirely separate and distinct. Specifically, the only commonality between methods is the underlying physical MARS principle. To further illustrate the effectiveness of P-MARS measurement and post-processing, Figure 11 contains an overlay of a contour plot of the far-field co-polar pattern of the x-band SGH measurement that was taken with (black contours) and without (red contours) the presence of the reflecting foil. Again the contours were plotted down to the -40 dB level with significant differences between the respective patterns being clearly evident. Conversely, Figure 13 contains an equivalent plot of the far-field only here P-MARS (second generation spherical implementation) processing has been applied to both patterns. Note that the same contour levels were used to generate Figures 10, 12 and 13. Clearly, the degree of agreement is very encouraging as demonstrated by the high degree similarity between the respective contour patterns.
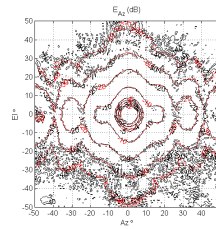

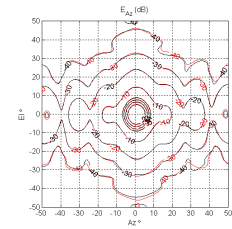**Figure 12 – SGH pattern without (red) and with (black) scatterer both without P-MARS.**

Figure 13 – SGH pattern without (red) and with (black) scatterer both with P-MARS.

Although not shown, a similar degree of agreement was attained between the respective cross-polarised patterns.

4. P-MARS Spatial Sampling Requirements

The adoption of a suitable spatial sampling scheme is absolutely essential if reliable far-field data are to be obtained. Conventionally, half wavelength spatial sampling is typically used in planar near-field antenna measurements as this satisfies the Nyquist sampling theorem in free space [8] in the absence of evanescent fields. However, it is common practice to adopt a finer spatial sampling criteria in circumstances when the measurements are taken in the presence of high levels of scattered fields, or if there are high levels of probe coupling which are being modulated by a periodic antenna structure. In the event there are high levels of scattered fields, the reflected fields can vary at a rate that is twice the half wavelength rate which results in the adoption of a conservative quarter wavelength sampling criteria being commonly adopted so as to insure that lobes that are associated with scattering are correctly placed outside of visible space, rather than appearing as spurious sidelobes in visible space as a result of aliasing. Indeed such phenomena are regularly assessed as part of the 18 term NIST range assessments [1]. As P-MARS is primarily utilised with scattering contaminated measurements, and as decreasing sample spacing correspondingly increases the amount of near-field data that must be acquired, obtaining conformation of the correct sampling requirement is of paramount importance if both accuracy and efficiency are to be maximised.

In order that spatial sampling could be examined, an x-band SGH was acquired in a multipath rich environment using three different x- and y-axis lattice spacings. These were, half wavelength (satisfy Nyquist for transmission measurements), quarter wavelength (satisfy Nyquist for reflection measurements) and eighth of a wavelength (over sampling). These data were transformed to the far-field using conventional planar processing and great circle cardinal cuts can be seen presented in Figure 14 below. The red, blue and black traces represent the half, quarter and eighth wavelength sample spacing measurements respectively. From inspection, and as would be expected, the far-field patterns are in good

agreement, with the half wavelength sampling case showing some differences at wide out angles, with the quarter and eighth wavelength sampling cases showing better agreement. This can perhaps be better illustrated by inspection of Figure 16. This plot presents the equivalent multipath levels (EMPL) [8] which were obtained by comparing each of the measurements. This can be thought of as the amplitude necessary to force the different pattern values to be exactly equal and is a measure of similarity. Here, it is clear that there is a greater degree of agreement between the quarter and eight wavelength sample spacing cases than between either of these measurements and the half wavelength sampled case.
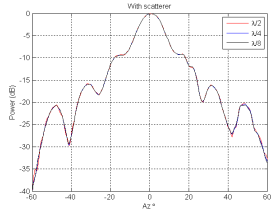

Figure 14 – Comparison of half, quarter and eighth wavelength sample spacing without P-MARS
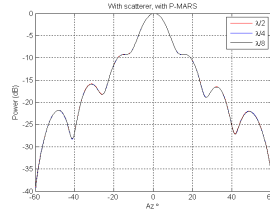

Figure 15 –. Comparison of half, quarter and eighth wavelength sample spacing with P-MARS
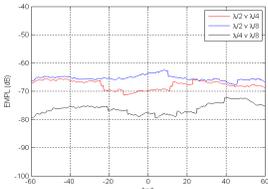

Figure 16 – EMPL plots showing agreement between patterns without P-MARS.
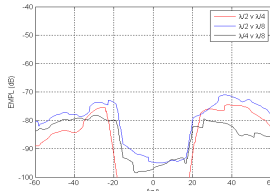

Figure 17 – EMPL plots showing agreement between patterns with P-MARS.

Figure, 15 contains an equivalent plot to Figure 14 only here, planar MARS has been used to supress the effect of the scattering on the respective far-field patterns. By inspection, and from Figure 17 (which presents an equivalent plot to Figure 16) it is apparent that each of these patterns are in equally good agreement. This would be expected since once the scattered fields have been removed from the patterns, the usual Nyquist half wavelength sampling should be sufficient to enable the complete field to be reconstructed from the samples. This is further corroborated as the Ordinal measure of adjacency and the Kendall measure of concordance were evaluated for each of these comparisons [8, 11] and can be found presented in Table 1 below. Here, the ordinal measure of adjacency constructs a measure of association which is based on the similarity of the permutations of the data when ranked in terms of the amplitude of the data sets, whereas the Kendall coefficient of concordance is based upon a measurement of the deviation of the ranked data sets from the mean rank of the data. These statistical measures of adjacency provide an objective commutative normalised measure of similarity where the greater the

degree of similarity the closer the coefficients are to unity. Two different ordinal statistics were used to provide additional conformation of the validity of the result.

Comparison	Ordinal	Kendall
k, $\lambda/2$ v $\lambda/4$	0.8906	0.9995
k, $\lambda/2$ v $\lambda/8$	0.8828	0.9993
k, $\lambda/4$ v $\lambda/8$	0.9688	0.9999
k, $\lambda/2$ v $\lambda/4$ (P-MARS)	0.9688	0.9999
k, $\lambda/2$ v $\lambda/8$ (P-MARS)	0.9531	0.9997
k, $\lambda/4$ v $\lambda/8$ (P-MARS)	0.9688	0.9999

Table 1: Measure of similarities between various sampling schemes using two different measures of adjacency.

From inspection of Table 1, it is evident that prior to P-MARS processing, the half wavelength spacing measurement was is poorest agreement whereas once P-MARS processing had been applied, all of the patterns were found to be in equally good agreement with one another. This observation is true irrespective of which coefficient of adjacency was used to assess the data. This implies that for a fixed near-field sampling interval, in the presence of scattering, reliable measurements can be taken in approximately half the time for the case where P-MARS processing is to be used than if conventional planar processing alone is used. Ordinal assessments were utilised as purely interval assessments were found to be saturated by the large dynamic range of the data and the very high degree of similarity exhibited thereby rendering these techniques, generally, less discriminatory in this area of application.

5. P-MARS Processing of Truncated Measurements

Truncation is the term given to the error that results when measurements are taken that sample only a portion of the total radiated near-field [1, 8]. In practice, conventional planar near-field measurements are always truncated to some degree as measurements cannot be taken in the aperture of the AUT, and only finitely large planar sampling intervals can be used. Thus, scattering contaminated measurements will always contain ripple resulting from spectral leakage which is caused by omitting some radiated near-fields. The impact that this has on a far-field pattern can be broadly divided into a first and second order truncation effect. The first order effect is that outside a given angle [1, 8] the uncertainty in the far-field pattern tends towards infinity, and secondly, that the ripple arising from Gibb's phenomena, *i.e.* missing plane wave spectra, give rise to high angular frequency ripple over all angles. In order that this could be investigated, a near-field measurement was taken that used a measurement interval that was as large as practicable. This data was then transformed to the far-field and then processed using P-MARS. The near-field data was then truncated by removing the five outermost rings of near-field data. This truncated dataset was

transformed to the far-field and plotted against the baseline data set. This was repeated for the case where successively 10, 15 and 20 outermost rings of data were truncated. Figure 18 below contains a plot of the far-field patterns as obtained using conventional planar processing. Vertical bars have been overlaid on the plots that illustrate the estimated onset of the first order truncation effect. Here, it is clear that as the near-field data is progressively truncated, the wide out pattern is attenuated and the amount of high angular frequency ripple increases, effecting sidelobes that are well within the maximum angular range.
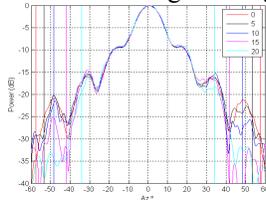

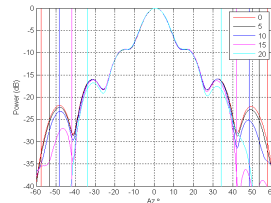**Figure 18 –. Without P-MARS**   **Figure 19 –. With P-MARS**

Figure 19 contains an equivalent plot to that of Figure 18 only here the data have been processed using the P-MARS algorithm. Encouragingly, from inspection of these patterns it is evident that the P-MARS processed far-field patterns provide representative far-field data even in the case where the near-field data set is grossly truncated. It is also clear that the high frequency ripple that was evident in the conventional far-field patterns has been effectively suppressed, thereby easing the impact of the spectral leakage (Gibb's ripple). This result would perhaps be anticipated as the P-MARS algorithm limits fluctuations in the pattern to those that can be physically induced by a current source of the prescribed electrical size. As spectral leakage is a high angular frequency ripple this would correspond to a current source of large size, specifically, a size which is greater than that permitted by the MARS algorithm. Therefore, MARS processing attenuates those effects arising from the second order truncation effect (MARS processing has no effect on the first order truncation effect).

6. Summary and Conclusions

Planar MARS processing can be used with a very high degree of confidence since all the steps in the measurement and analysis are consistent with the well-established principles of standard near-field theory and measurement technique, and all comparisons thus far have proved overwhelmingly positive. The offset of the AUT and the resulting larger sampling interval are estimated using conventional rules, and the mathematical translation of the AUT to the origin is rigorous. The selection of the mode cut-off for the translated pattern is based on the physical dimensions of the AUT and its translated location. The final result with MARS processing can be degraded if the sampling area of the near-field data is too restrictive, or the mode filter is too

tight, *i.e.* abrupt, but importantly these parameters are controlled by the user. The results of planar MARS processing will reduce but cannot entirely eliminate the effect of scattering. As has been demonstrated previously, this novel frequency domain measurement and processing technique is entirely general and can be used to achieve acceptable results with use of minimal absorber or even without the use of an anechoic chamber, even when testing lower gain antennas. MARS has been found to improve the reflection levels in traditional anechoic chambers allowing improved accuracy as well as offering the ability to use existing chambers down to lower frequencies than the absorber might otherwise suggest. Additional validation of P-MARS post processing has been provided and presented by means of an entirely independent, novel, SWE based formulation and implementation of the P-MARS algorithm. Sampling requirements have been investigated and an optimum presented.

7. REFERENCES

[1] A.C. Newell, "Error Analysis Techniques for Planar Near-field Measurements", IEEE Transactions on Antennas and Propagation, vol. AP-36, pp. 754-768, June 1988.

[2] G.E. Hindman, A.C. Newell, "Reflection Suppression in a large spherical near-field range", AMTA 27th Annual Meeting & Symposium, Newport, RI, October. 2005.

[3] G.E. Hindman, A.C. Newell, "Reflection Suppression To Improve Anechoic Chamber Performance", AMTA Europe 2006, Munich, Germany, March 2006.

[4] S.F. Gregson, A.C. Newell, G.E. Hindman, "Reflection Suppression in Cylindrical Near-Field Antenna Measurement Systems – Cylindrical MARS", AMTA 31st Annual Meeting & Symposium, Salt Lake City, UT, November 2009.

[5] S.F. Gregson, A.C. Newell, G.E. Hindman, M.J. Carey, "Advances in Cylindrical Mathematical Absorber Reflection Suppression", 4th European Conference on Antennas and Propagation, Barcelona, 12th - 16th April, 2010.

[6] S.F. Gregson, A.C. Newell, G.E. Hindman, M.J. Carey, "Extension of The Mathematical Absorber Reflection Suppression Technique To The Planar Near-Field Geometry", AMTA, Atlanta, October 2010.

[7] S.F. Gregson, A.C. Newell, G.E. Hindman, M.J. Carey, "Application of Mathematical Absorber Reflection Suppression to Planar Near-Field Antenna Measurements", 5th European Conference on Antennas and Propagation, EuCAP 2011, Rome, April 2011.

[8] S.F. Gregson, J. McCormick, C.G. Parini, "Principles of Planar Near-Field Antenna Measurements", IET, UK, 2007.

[9] D.M. Kerns, "Plane-Wave Scattering-Matrix Theory Of Antennas And Antenna-Antenna Interactions", Nat. Bur. Stand. (U.S.) Monograph 162, June 1981.

[10] J.E. Hansen, Ed., "Spherical Near-Field Antenna Measurements", IEE, UK, 1988.

[11] J. McCormick, S.F. Gregson, C.G. Parini, "The Use of Statistical Image Classification Techniques for the Assessment of Measured Antenna Pattern Functions", 5th European Conference on Antennas and Propagation, EuCAP 2011, Rome, April 2011.